

Determination of physical properties of the asteroid (41) Daphne from interferometric observations in the thermal infrared [☆]

Alexis Matter^{a,1,*}, Marco Delbo^b, Sebastiano Ligori^c, Nicolas Crouzet^{b,2},
Paolo Tanga^b

^a*UNS-CNRS-Observatoire de la Côte d'Azur, Laboratoire Fizeau, BP 4229 06304 Nice
cedex 04, France.*

^b*UNS-CNRS-Observatoire de la Côte d'Azur, Laboratoire Cassiopée, BP 4229 06304 Nice
cedex 04, France.*

^c*INAF-Osservatorio Astronomico di Torino, Strada Osservatorio 20, 10025 Pino Torinese,
Torino, Italy.*

Number of pages: 44

Number of tables: 3

Number of figures: 8

[☆]Based on observations collected at the European Southern Observatory (ESO), Chile:
ESO Program ID 080.C-0195, VISA-Italy.

*Corresponding author.

Email address: amatter@mpifr-bonn.mpg.de (Alexis Matter)

¹Present address: Max-Planck Institut für Radioastronomie, Auf dem Hügel 69, 53121
Bonn, Germany.

²Present address: Space Telescope Science Institute, 3700 San Martin Drive, Baltimore,
MD 21218, USA.

Proposed running head: Asteroid interferometry in the thermal IR.

Editorial correspondence and proofs should be directed to:

Alexis Matter

Max-Planck Institut für Radioastronomie,
Auf dem Hügel 69, 53121 Bonn, Germany.

email: amatter@mpifr-bonn.mpg.de;

Tel: +49 228 525 186

Fax: +49 228 525 229

Abstract

1 We describe interferometric observations of the asteroid (41) Daphne in
2 the thermal infrared obtained with the Mid-Infrared Interferometric Instrument
3 (MIDI) and the Auxiliary Telescopes (ATs) of the European Southern Obser-
4 vatory (ESO) Very Large Telescope Interferometer (VLTI). We derived the size
5 and the surface thermal properties of (41) Daphne by means of a thermophysical
6 model (TPM), which is used for the interpretation of interferometric data for the
7 first time. From our TPM analysis, we derived a volume equivalent diameter for
8 (41) Daphne of 189 km, using a non-convex 3-D shape model derived from op-
9 tical lightcurves and adaptive optics images (B. Carry, private communication).
10 On the other hand, when using the convex shape of Kaasalainen et al. (2002.
11 Icarus 159, 369–395) in our TPM analysis, the resulting volume equivalent di-
12 ameter of (41) Daphne is between 194 and 209 km, depending on the surface
13 roughness. The shape of the asteroid is used as an *a priori* information in our
14 TPM analysis. No attempt is made to adjust the shape to the data. Only the
15 size of the asteroid and its thermal parameters such as, albedo, thermal inertia
16 and roughness are adjusted to the data. We estimated our model systematic
17 uncertainty to be of 4% and of 7% on the determination of the asteroid volume
18 equivalent diameter depending on whether the non-convex or the convex shape
19 is used, respectively. In terms of thermal properties, we derived a value of the
20 surface thermal inertia smaller than $50 J m^{-2} s^{-0.5} K^{-1}$ and preferably in the
21 range between 0 and $\sim 30 J m^{-2} s^{-0.5} K^{-1}$. Our TPM analysis also shows
22 that Daphne has a moderate macroscopic surface roughness.

²³ **Keywords**

²⁴ Asteroids; Asteroids surfaces; Infrared observations; Data reduction techniques.

25 1. Introduction

26 Information about sizes and shapes of asteroids provides essential constraints
27 to the history and formation processes of these bodies (Bottke et al., 2005;
28 Tanga et al., 2009). The size distribution of the different subpopulations of as-
29 teroids and of the asteroid dynamical families constrain the collisional evolution
30 processes that these bodies have experienced during their history (Bottke et al.,
31 2005). Moreover, accurate determination of sizes and shapes is crucial to es-
32 timate volumes of asteroids, which allow one to calculate the bulk densities of
33 these bodies when their masses are determined by some means. The density and
34 internal structure are among the most important characteristics of asteroids, yet
35 they are also some of the least constrained. When compared with the densities
36 of meteorites - a partial sample of the building blocks of asteroids that survive
37 the passage through the Earth's atmosphere - one can deduce the nature of
38 asteroid interiors. These physical properties of asteroids reflect the accretional
39 and collisional environment of the early solar system.

40 The determination of the volumes of asteroids will be particularly important
41 in the next future when more asteroid masses are expected to be accurately de-
42 rived. For instance, it has been estimated that the masses of slightly more
43 than 100 asteroids will be determined to better than 30% (relative accuracy)
44 from the gravitational perturbations that these bodies exert on the orbits of
45 smaller asteroids thanks to the high accuracy astrometric measurements of the
46 ESA space mission Gaia (launch in 2013; Mouret et al., 2007). Yet, the volume
47 of these bodies are not known with accuracies small enough to allow one to
48 calculate meaningful densities. The volumes of asteroids are affected by large
49 errors because their true 3-dimensional shapes are generally unknown and thus
50 approximated by means of spheres. It can be noted, for instance that by using
51 a shape and a spin solution derived from lightcurves and mutual occultation
52 events for the asteroid (22) Kalliope, Descamps et al. (2008) significantly re-
53 visited its volume and thus its density compared to previous estimates based on
54 a sphere. The error in the estimation of the volume can also be significant when

55 large scale topographic concavities, known to be present on asteroids (see e.g.,
56 Thomas et al., 1999, 2002), are approximated with flat surfaces.

57

58 From the size (D) and the absolute magnitude of an asteroid in the visible
59 light (H), one can derive the geometric visible albedo (p_V) using the formula:

$$D(km) = 1329 p_V^{-1/2} 10^{-H/5}. \quad (1)$$

60 The value of the albedo is important to constrain the nature of asteroids: it is
61 known, for instance, that asteroids with spectra similar to carbonaceous chon-
62 drite meteorites (types CI and CM), the so-called C-type asteroids, have values
63 of p_V between 0.03 and 0.10 (Stuart and Binzel, 2004); stony (S-type) asteroids,
64 rich in silicates such as olivine and pyroxene have moderate values of p_V (e.g.,
65 between ~ 0.15 and ~ 0.3) (Stuart and Binzel, 2004), whereas asteroids whose re-
66 flectance spectrum is analog to that of enstatite meteorites are known to have in
67 general high (> 0.4) albedo values (see e.g., Tedesco et al., 1989, and references
68 therein). In general sizes and albedos of asteroids are obtained from photometric
69 observations of these bodies in the thermal infrared (see Harris and Lagerros,
70 2002, for a review on the topic). Models of the surface temperature distribution
71 and the corresponding infrared emission are used for the analysis of observa-
72 tional data (Delbo and Harris, 2002; Harris and Lagerros, 2002). In particular,
73 thermophysical models (TPM) take explicitly into account the effects of thermal
74 inertia, spin state, asteroid shape and surface roughness on the calculation of
75 asteroids infrared emission.

76 One of these parameters, the thermal inertia, a measure of the resistance of
77 a material to temperature change, is particularly important. It is defined by
78 $\Gamma = \sqrt{\rho\kappa c}$, where κ is the thermal conductivity, ρ the density and c the specific
79 heat. The value of the thermal inertia depends on the material properties (see
80 Mueller, 2007, and references therein for a table of thermal inertia values of
81 some typical materials) and inform us about the nature of the surface regolith:
82 a soil with a very low value of Γ , for instance in the range between 20 and 50
83 $J m^{-2} s^{-0.5} K^{-1}$, is covered with fine dust; an intermediate value (150-700

84 $J m^{-2} s^{-0.5} K^{-1}$) indicates a coarser, mm- to cm-sized, regolith as observed
85 on (433) Eros (Veveřka et al., 2001a,b) and (25143) Itokawa (Yano et al., 2006),
86 respectively; solid rock with very little porosity is known to have thermal inertia
87 values of more than $2500 J m^{-2} s^{-0.5} K^{-1}$ (Jakosky, 1986). The correlation
88 between the value of Γ and the nature of the soil has been also demonstrated
89 from study of the martian surface (see e.g., Christensen et al., 2003). More-
90 over, because thermal inertia controls the surface temperature distribution of
91 an asteroid, it affects the strength of the Yarkovsky effect. This is the gradual
92 drifting of the semi major axis of the orbits of km-sized asteroids caused by the
93 asymmetric (with respect to the direction asteroid-sun) emission of the thermal
94 infrared radiation that carry momentum (see Bottke et al., 2006, and references
95 therein). This effect plays a role in the delivery of near-Earth asteroids from
96 the main belt (Morbidelli and Vokrouhlický, 2003), in the dispersion of aster-
97 oid families (Nesvorný and Bottke, 2004), and it is a major source of uncer-
98 tainty in the impact prediction estimations for potentially hazardous asteroids
99 (Giorgini et al., 2002; Milani et al., 2009). Finally, accurate determination of
100 thermal inertia is important in the estimation of systematic errors on sizes and
101 albedos of asteroids, when these parameters are determined by means of simple
102 thermal models (see e.g., Spencer et al., 1989).

103 As shown by Delbo et al. (2009), the Very Large Telescope Interferometer
104 (VLTI) of the European Southern Observatory (ESO) can be used to obtain
105 measurements of asteroid sizes and shapes. Generally speaking, the VLTI has
106 the ability of measuring directly sizes and deriving rough information about the
107 shape of asteroids from measurements of the visibility (contrast) of interfero-
108 metric fringes. The visibility is a function of the apparent angular extension of
109 the body along the projected interferometer baseline. Shape features such as
110 large concavities, bilobed shapes and/or presence of satellites, also produce a
111 clear signature in the visibility. A sensitive instrument to measure asteroid vis-
112 ibilities at the VLTI in the mid-infrared N-band (8-13 μm) is the Mid-Infrared
113 Interferometric Instrument (MIDI; Leinert et al., 2003). The angular resolv-

114 ing power of the interferometer depends on the length of the baseline. VLTI
115 baselines vary between 16 and 130 m, with theoretical corresponding angular
116 resolutions between 130 and 16 mas (milliarcseconds) at 10 μm .

117 Interferometric observations of asteroids with other facilities, such as the
118 Fine Guidance Sensors (FGS) of the Hubble Space Telescope (HST, Tanga et al.,
119 2001; Hestroffer et al., 2002; Tanga et al., 2003), demonstrated the capability of
120 the method of obtaining sizes of asteroids and reconstructing the ellipsoids that
121 best fit their shape. Given the limiting magnitude of the FGS, only bright
122 ($V \leq 12$) and large (~ 100 km-sized) asteroids were observed by this program.
123 However, only the large VLTI baselines can overcome these sensitivity and size
124 limitations by extending the use of the interferometric technique to a large
125 number of fainter and smaller targets. One particularly interesting feature of the
126 MIDI instrument is that it also measures the total (non coherent) spectral energy
127 distribution, $I(\lambda)$, of the source in the 8-13 μm spectral interval. This thermal
128 infrared data can then be used as a further constraint to derive asteroid sizes,
129 through the application of asteroid thermal models. In their work, Delbo et al.
130 (2009) show the first successful interferometric observations of two asteroids
131 with MIDI, (234) Barbara and (951) Gaspra.

132 In this work, we report on the continuation of the program devoted to mea-
133 surement of the physical properties of asteroids from interferometric observa-
134 tions in the thermal infrared. In particular, we obtained the first successful
135 interferometric observations of asteroids using the Auxiliary Telescopes (ATs)
136 of the VLTI. From fluxes and interferometric visibilities measured in the ther-
137 mal infrared, we derived the size of the asteroid (41) Daphne, and we studied
138 its thermal properties by means of a TPM.

139 This work is structured as follows: in section 2 we detail the thermophysical
140 model used for the interpretation of MIDI data in terms of asteroid physical
141 properties; in section 3 we report the observations and the data reduction pro-
142 cess that we adopted; in section 4, we detail the shape models that we used; in
143 section 5, we give our results, followed by a discussion in section 6.

144 2. Modeling and analysis of MIDI observations

145 MIDI is used to coherently combine the infrared light collected by two of
146 the four 8-m Unit Telescopes (UT) or by two of the four 1.8-m Auxiliary Tele-
147 scopes (AT) of the ESO VLTI. The two observables measured by MIDI are the
148 photometric flux $I(\lambda)$ and the visibility $V(u, v)$ of the source; where $u = B_x/\lambda$
149 and $v = B_y/\lambda$ are the spatial frequencies in rad^{-1} along the x- and y-axis, with
150 B_x and B_y the components, along the two axis, of the interferometer's baseline,
151 projected on the plane of the sky. The x and y-axis define the coordinates on
152 this plane. We recall that $V(u, v)$ is the Fourier transform of the brightness
153 distribution of the source divided by $I(\lambda)$. The visibility can be also indicated
154 with $V(\mathbf{B}/\lambda)$, where \mathbf{B} is a vector of components (B_x, B_y) .

155 Delbo et al. (2009) interpreted $I(\lambda)$ and $V(\mathbf{B}/\lambda)$ using simple thermal mod-
156 els and simple geometric models (disk of uniform brightness and system of two
157 disks) in order to derive the size of (951) Gaspra and (234) Barbara. For the
158 latter asteroid, a disk of uniform brightness poorly reproduced the observa-
159 tions, whereas a binary model provided a good fit to the data. For this reason
160 Delbo et al. (2009) speculated that Barbara has a bilobed shape or a satellite.
161 When we have *a priori* information about the shape and the spin state of an
162 asteroid, TPMs can be used to derive the size of the body and to constrain sur-
163 face properties, such as albedo and thermal inertia and macroscopic roughness.
164 These parameters are explicitly taken into account in the TPM to calculate
165 the asteroid's thermal emission, and are adjusted until model fluxes best fit si-
166 multaneously observations obtained at different epochs and wavelengths in the
167 thermal infrared. In general, these observations are measurements of the ob-
168 ject's disk integrated thermal infrared flux $I(\lambda)$ (see e.g., Müller and Barnes,
169 2007; Delbo and Tanga, 2009).

170 Here, we used a TPM to calculate interferometric visibilities of asteroids in
171 the thermal infrared for the first time. Our procedure consists in generating
172 images of the thermal infrared emission of the asteroid at different wavelengths
173 as viewed by the observer and then obtaining the model visibility and flux for

174 each image: the model flux is calculated by taking the integral of all pixels at
 175 each wavelength, while the model visibility is calculated as the modulus of the
 176 Fourier transform of the image, along the projected baseline direction, divided
 177 by the flux.

178 The free parameters of the TPM are adjusted in order to minimize the dis-
 179 tance between the disk integrated flux $I'(\lambda)$ and visibility $V'(\mathbf{B}/\lambda)$ of the model,
 180 and the corresponding observed quantities $I(\lambda)$ and $V(\mathbf{B}/\lambda)$. As goodness of
 181 the fit indicator, we use the reduced χ^2 , namely:

$$\bar{\chi}^2 = \frac{1}{N} \left[\sum_{i=1}^{N_e} \sum_{j=1}^{F_i} \left(\frac{I_i(\lambda_j) - I'_i(\lambda_j)}{\sigma_{I_{i,j}}} \right)^2 + \sum_{i=1}^{N_E} \sum_{j=1}^{W_i} \left(\frac{V_i(\mathbf{B}/\lambda_j) - V'_i(\mathbf{B}/\lambda_j)}{\sigma_{V_{i,j}}} \right)^2 \right] \quad (2)$$

182 where the indexes i and j run over the observation epochs and the discrete
 183 samples in wavelength at which the visibility and the flux were measured, N_e
 184 and N_E are the number of epochs at which flux and visibility are respectively
 185 measured, F_i and W_i are the number of flux and visibility samples at the i^{th}
 186 epoch, $N = \sum_{i=1}^{N_e} N_{\lambda,I}^i + \sum_{i=1}^{N_E} N_{\lambda,V}^i$ is the total number of measurements,
 187 and $\sigma_{V_{i,j}}$ and $\sigma_{I_{i,j}}$ are the uncertainties on the measured visibilities and fluxes,
 188 respectively.

189 The physical parameters of our TPM, are:

- 190 • An *a priori* information about the shape of the body, described by a mesh
 191 of planar triangular facets and the spin vector of the asteroid. The shape
 192 and the spin vector are in general determined by lightcurve inversion (see
 193 Kaasalainen et al., 2002, for a review), disk-resolved imaging (from e.g.,
 194 *in-situ*, the Hubble Space Telescope, and/or ground-based adaptive optics
 195 observations; see e.g., Carry et al., 2010), or radar (see e.g., Ostro et al.,
 196 2000). Our implementation of the TPM allows non-convex shapes to be
 197 used. Shadowing of facets to the observer due to the body's topography
 198 is fully taken into account. Mutual heating and light reflection between
 199 facets within topographic concavities are not modeled in this version of the
 200 TPM. However, their effect is of second order on the surface temperature

201 determination. The spin vector solution is given by the rotational phase
 202 ϕ_0 at a reference epoch t_0 , the ecliptic longitude λ_0 and latitude β_0 of the
 203 spin axis direction, and the rotation period P . Note that t_0 can be quite
 204 far in the past. As a consequence, the absolute rotational phase, $\phi(t)$, of
 205 the asteroid, at a more recent epoch (e.g., the time of VLTI observations),
 206 can be affected by a significant uncertainty, Δ_ϕ . The latter depends on
 207 the error σ_P on P , the value of P , and by how far t is from t_0 . Since
 208 $\phi = \phi_0 + 2\pi(t - t_0)P^{-1}$, we can write that

$$\Delta_\phi = 2\pi(t - t_0)P^{-2}\sigma_P, \quad (3)$$

209 neglecting the error on ϕ_0 (which is safe - in general - to assume small).
 210 When $\Delta_\phi \gtrsim 10^\circ$, then Δ_ϕ should be treated as a free parameter of the
 211 TPM.

- 212 • The size of the body. This is described by a factor a that linearly scales
 213 all vertexes of the mesh. We give the size of the body in terms of the
 214 diameter of the sphere of equivalent volume $D_V = 2 \left(\frac{3V}{4\pi}\right)^{\frac{1}{3}}$, where V is the
 215 volume of the mesh.
- 216 • The bolometric Bond's albedo A . This is related to p_V via the relation:
 217 $A = p_V(0.29 + 0.684G)$, where G is the slope parameter of the H, G sys-
 218 tem of [Bowell et al. \(1989\)](#). Although the value reported in the MPC for
 219 (41) Daphne is 0.10, the use of the typical default value, namely $G=0.15$
 220 ([Bowell et al., 1989](#)), does not significantly affect our results and we de-
 221 cided to keep it.
- 222 • The macroscopic surface roughness. This is modeled by adding hemi-
 223 spherical craters of opening angle, γ_c , and surface density, ρ_c . Following
 224 [Delbo and Tanga \(2009\)](#), we used here four preset combinations of γ_c and
 225 ρ_c spanning the range of possible values of surface roughness. These values
 226 of macroscopic roughness are given in [Table 1](#), including the corresponding
 227 value of the mean surface slope, $\bar{\theta}$, as defined by [Hapke \(1984\)](#).

- The value of thermal inertia, which affects the temperature of each tile of the mesh and the temperature distribution inside craters.

Albedo, thermal inertia, and roughness are assumed constant over the surface of the body.

[Table 1 here]

In order to compute images of the model thermal emission, the first step is to use the TPM to calculate the body’s surface temperature distribution, namely the temperature of each tile of the mesh and inside craters at any given epoch t . This is performed by solving the one-dimensional heat diffusion equation for each tile of the mesh (see Mueller, 2007, for more details). The boundary conditions of the heat diffusion equation are given, at the surface, by the input radiative heating from the Sun and irradiation of the heat into space, and, at depth, by imposing a zero net heat flow towards the interior of the body. The position of the Sun (the heat source) with respect to each facet is calculated by applying the inverse coordinates transformations of Durech et al. (2010) in order to transform the heliocentric position vector of the asteroid into the body’s mesh reference frame: the transformation is a function of the time t . The method we adopt to calculate the temperature distribution inside craters is given by Emery et al. (1998). We do not explicitly model thermal conduction inside craters, and here we use the approximation of Lagerros (1998). This approximation cannot be used on the night side. However, this is not a limitation for the present study because our observations took place at a moderate solar phase angle (see Table 2). Consequently, the fraction of the night side seen by the observer was negligible. Because of the finite thermal inertia value, the heat diffusion is not instantaneous and the body temperature distribution depends on his past illumination history. For this reason, the calculation of the heat diffusion is started ~ 100 rotations (\sim a month) before the observation epochs. We carefully checked that the body temperature distribution stabilizes and is inde-

258 pendent of the initial conditions. From the knowledge of the body temperature
 259 distribution, model fluxes are calculated assuming a wavelength independent
 260 emissivity of 0.9, for each tile of the mesh, including craters, in the direction
 261 towards the observer. The emissivity of 0.9 assumed here is typical for the vast
 262 majority of silicate powders. The emissivity of these materials is within 10% of
 263 0.9 in the wavelength range between 7 and 14 μm (see e.g., Mueller, 2007, and
 264 references therein). Then the three-dimensional mesh is projected on the plane
 265 of the sky to create a two dimensional image of the asteroid. In order to have
 266 a reasonable image size, while remaining close to the maximum resolution of
 267 the MIDI instrument, we sampled the images with a resolution of 4 mas/pixel
 268 (5 mas/pixels for the convex shape of 41 Daphne; see section 5). Our results
 269 are robust with respect to changes of the pixel scale. The value of each pixel is
 270 calculated from the flux of the facet of the mesh on which the pixel is projected
 271 to: namely it is the facet flux multiplied by the area of the pixel and divided
 272 by the projected area of the facet. Fig. 1 shows two images of (41) Daphne
 273 obtained along the lines described above, from the two shape models described
 274 later. These images are created for each wavelength.

275

276 **[Fig. 1 here]**

277

278 Then the integrated flux and visibility of the model are given by:

$$I'(\lambda_j) = a^2 \sum_{x,y} O'(x, y, \lambda_j) \quad (4)$$

$$\begin{aligned}
 V' \left(\frac{B}{\lambda_j} \right) &= \frac{FT(O'(\frac{x'}{a}, \frac{y'}{a}, \lambda_j))}{I'(\lambda_j)} = \frac{a \hat{O}'(\frac{aB}{\lambda_j})}{I'(\lambda_j)} \\
 &= \frac{a}{I'(\lambda_j)} \sum_{y'} \left(\sum_{x'} O'(x', y', \lambda_j) \right) e^{\frac{-i2\pi aB}{\lambda_j} y'} \quad (5)
 \end{aligned}$$

279 where FT is the Fourier Transform operator applied to the brightness distribu-
 280 tion of the asteroid O' , (x', y') is a system of coordinates rotated by an angle PA
 281 with respect to the (x, y) frame. The y' axis thus coincides with the direction

282 of the baseline (see Fig. 2) so that we replace the baseline vector, noted \mathbf{B} , by
 283 its modulus, noted B , in the expression of the model visibility above. $N_{y'}$ is
 284 the number of pixels in the image along the y' axis. In Eqs. 4 and 5, we have
 285 explicitly written the dependence of the flux and the visibility on the mesh scale
 286 factor a . It is important to note that changing the scale of an object by a linear
 287 factor a is equivalent to multiply the baseline length by a factor a , or inversely.

288

289 **[Fig. 2 here]**

290

291 The free parameters of the TPM are: size (which is varied through the scale
 292 factor a), thermal inertia, and macroscopic surface roughness. The fit procedure
 293 involves calculation of $I'_i(\lambda_j)$ and $V'_i(B/\lambda_j)$ at each observing epoch and each
 294 wavelength λ_j , for a number of discrete values of Γ and macroscopic surface
 295 roughness. Note that the dependence of the $\bar{\chi}^2$ on a is trivial, as it can be seen
 296 from Eqs. 4 and 5. Thus, the best value of a for each discrete value of Γ and
 297 each roughness model can be found by minimizing the Eq. 2. Then, the location
 298 of the minimum $\bar{\chi}^2$ as function of Γ gives the best-fit asteroid surface thermal
 299 inertia for each roughness model. Eventually, the value of a at Γ -minimum is
 300 used to determine the best-fit value of D_V .

301 In some cases, the correction to the rotational phase Δ_ϕ has to be treated as
 302 a free parameter of the TPM. In this case, the location of the minimum $\bar{\chi}^2$, as a
 303 function of Δ_ϕ for different roughness and thermal inertia values, gives the set
 304 of best-fit physical parameters for the asteroid. An optical lightcurve obtained
 305 quasi-simultaneously could help reduce Δ_ϕ .

306

307 In the next section, we describe our observations of the asteroid (41) Daphne
 308 and the related data reduction.

309 **3. Observations and data reduction**

310 The observations of (41) Daphne were carried out in service mode, on 2008
311 March 12 and 14 . We adopted the typical observing sequence with MIDI,
312 which is extensively described by Przygodda et al. (2003). Using two ATs in
313 the E0-G0 baseline configuration ($B = 16$ m), we acquired four visibility obser-
314 vations for (41) Daphne, two on March 12 and two on March 14. Table 2 reports
315 the observational circumstances. The telescopes and the delay lines of the inter-
316 ferometer were tracked at the rates predicted from the ephemerides of the target.

317

318 **[Table. 2 here]**

319

320 Our observations included a mid-infrared photometric and interferometric
321 calibrator chosen from the ESO database, namely HD123139. The absolutely
322 calibrated infrared spectrum of the calibration star was taken from Cohen
323 (1999). Extraction and calibration of the visibility measurements of (41) Daphne
324 were performed using the same method as Delbo et al. (2009). The flux and vis-
325 ibility measurements of (41) Daphne are shown in Fig 3 (or identically in Fig 4).
326 The estimation of error bars constitutes a difficult issue when reducing MIDI
327 data. In the most common case, when the ‘high-sensitivity’ mode is used, the
328 photometry is acquired about 3 to 6 minutes after the fringes are recorded.
329 Therefore, the measured value of $I(\lambda)$ does not correspond to the flux of the
330 source at the time of the fringes recording. This leads to typical uncertainties
331 of about 10 to 15% (see Chesneau, 2007, for more details). This error strongly
332 depends on the atmospheric conditions during the night. An estimation of the
333 error bars can thus be obtained by computing the RMS of the visibilities val-
334 ues of several calibrators observed closely to the source (or identically several
335 observations of the same calibrator). We used this procedure for the two first
336 visibilities, and considered a typical relative uncertainty of 15% for the two
337 others since only one calibrator was observed during the second night.

338 **[Fig. 3 and Fig. 4 here]**

339

340 In addition to the interferometric observations, we obtained an optical lightcurve
341 of (41) Daphne, in order to better constrain the rotational phase at the epoch
342 of the VLTI observations. In October 2009, during the tests of the 0.4 m
343 telescope for the Antarctic Search for Transiting ExoPlanets (ASTEP) project
344 (Daban et al., 2010) at the Observatoire de la Côte d’Azur in Nice, France, we
345 performed time-resolved CCD photometric observations of this asteroid in the
346 visible. Our observations spanned a period of about 3 h. We used the technique
347 of differential photometry, which makes use of stars present in the same CCD
348 frame as the target, to allow for accurate removal of systematic effects such as
349 atmospheric extinction variability. The telescope was tracked at the sidereal
350 rate. The reduction of the CCD frames consisted in the conventional bias re-
351 moval and flat-fielding, which was performed by using bias and flat calibration
352 frames. The corresponding lightcurve is shown in Fig. 5, where the times of the
353 observations were light-travel subtracted.

354

355 **[Fig. 5 here]**

356

357 In the next section we describe the different shape models used for (41)
358 Daphne, and how the TPM analysis was performed using this information).

359 **4. Shape models and TPM analysis**

360 For sake of comparison and evaluation of the results variability, two shape
361 models were used in this study:

- 362 1. a convex mesh was downloaded (March 2010) from the Database of Aster-
363 oid Models from Inversion Techniques or DAMIT (see Durech et al., 2010,
364 and http://astro.troja.mff.cuni.cz/projects/asteroids3D/web.php?page=project_main_page).
365 This is a database of three-dimensional models of asteroids derived by
366 solving the inverse problem of determining the object’s shape and its ro-
367 tational state from optical lightcurves. It also lists some models derived

368 from a combination of adaptive optics images and lightcurves. The convex
369 shape of (41) Daphne contains 1022 vertexes and 2040 triangular planar
370 facets. The pole solution is also given: $\lambda_0=198^\circ$ $\beta_0=-32^\circ$, $P=5.98798$ h,
371 $\phi_0=0^\circ$ at the reference epoch $t_0=2444771.79382$ (JD);

372 2. the second shape model of (41) Daphne, provided by B. Carry (private
373 communication)³, is non-convex and was derived from the KOALA method
374 (Carry et al., 2010; Kaasalainen, 2011). We recall here that this method
375 allows one to derive the size and the shape of an asteroid from the inversion
376 of data obtained by different observational techniques: namely, photomet-
377 ric lightcurves and adaptive optics images in the case of (41) Daphne. The
378 corresponding pole solution is: $\lambda_0=198^\circ$ $\beta_0=-31^\circ$, $P=5.987980$ h, $\phi_0=0^\circ$
379 at the reference epoch $t_0= 2444771.79382$ (JD).

380 Note that, while the size of the first shape model is arbitrary, the non-convex
381 shape, derived from the KOALA method, has a volume equivalent diameter of
382 $D_V = 185 \pm 5$ km. We call it ‘the nominal size’ in the following. The pole
383 solution of the convex model of (41) Daphne was obtained from inversion of a
384 set of 23 optical lightcurves obtained in the period 1976 - 1988. Assuming $t_0 =$
385 December 21, 1988 and $\sigma_P=0.00001$ hours, we thus find that $\Delta_\phi \sim 17^\circ$ at the
386 epoch of our VLTI observations, given the rotation period of 5.98798 hours for
387 this object. As a consequence, we attempted to better constrain the rotational
388 phase of (41) Daphne using our recently obtained lightcurve shown in Fig. 5.
389 To do so, we calculated synthetic visible lightcurves using the convex shape of
390 (41) Daphne and attempted to fit the model to the observed lightcurve using
391 the value of Δ_ϕ as a free parameter. A geometric scattering model was adopted:
392 namely the visible reflected flux from each facet is proportional to the projected
393 area of the facet, and it is required that the facet is also illuminated by the
394 sun. Fig. 5 also shows the best fit model lightcurve that we obtained using the
395 convex model for a correction value of $\Delta_\phi = (-0.2 \pm 0.3)^\circ$. The correction to

³See also his PHD thesis manuscript available at <http://benoit.carry.free.fr/> for further information.

396 the nominal rotational phase is thus negligible.

397 For the non-convex model, given that the KOALA model uses recent observa-
398 tions from 2008 March 28, and that the period is more accurate (by an order
399 of magnitude), the error on the rotational phase given by the pole solution is
400 negligible as well. As a consequence, for the two shape models, the rotational
401 phase was not treated as a free parameter. The TPM was run for each roughness
402 model (see Table 1), and each value of thermal inertia, namely 0, 5, 10, 25, 50,
403 75, 100, 150, 200, 300, 400 and $500 J m^{-2} s^{-0.5} K^{-1}$. Then the fit procedure
404 described in section 2 was applied to the measured fluxes and visibilities.

405 In the next section we describe and discuss the results obtained from the
406 application of the TPM to the observed visibilities and fluxes of (41) Daphne.

407 5. Results

408 5.1. Convex shape model

409 Fig. 6 shows our best-fit estimator $\overline{\chi^2}$ as a function of Γ for the four different
410 roughness models, in the case of the convex shape.

411

412 **[Fig. 6 here]**

413

414 We note that a surface with a low or no macroscopic roughness and a value of
415 thermal inertia $< 100 J m^{-2} s^{-0.5} K^{-1}$ gives the best fit to the observations.

416 In particular the minima of the ‘no roughness’ and ‘low roughness’ models are
417 at $\Gamma=48$ and $8 J m^{-2} s^{-0.5} K^{-1}$, respectively. The corresponding values of D_V
418 are 209 and 194 km, with associated p_V values of 0.057 and 0.067, respectively.

419 In Fig. 3 we plot the visibility and flux of the best-fit model (‘no roughness’, $\Gamma =$
420 $48 J m^{-2} s^{-0.5} K^{-1}$, $D_V = 209$ km, $p_V = 0.057$), in addition to the measured
421 fluxes and visibilities of (41) Daphne. We note that our model represents well
422 the observed flux except for the third observing epoch, where the flux of the
423 TPM is greater than the measured one (by roughly 20% at $13 \mu\text{m}$). This ‘offset-
424 like’ mismatch may likely come from an underestimation of the source flux by

425 MIDI, especially around $13 \mu\text{m}$ where the signal to noise ratio is generally quite
 426 low (Chesneau, 2007). The photometry measurement of the source may thus be
 427 degraded by a bad estimation and suppression of the thermal background (and
 428 its fluctuations), which is dominant in the mid-infrared (see e.g., Perrin et al.,
 429 2003). Moreover, the underestimation of the flux at the third epoch implies a
 430 similar offset-like mismatch between the corresponding measured and calculated
 431 visibilities at the same epoch.

432 In order to estimate the statistical uncertainty affecting the fit parameters
 433 Γ and D_V , a Monte-Carlo analysis was performed. To this end, 200 normally
 434 distributed flux and visibility values per observation were generated at each
 435 wavelength, with average and standard deviation matching the measured fluxes
 436 and visibilities within their respective $1 - \sigma$ uncertainty. For each set of fluxes
 437 and visibilities, a fit of the model, as described in section 2, was performed.
 438 Then, we took the standard deviation of the Γ and D_V values at the minimum
 439 $\bar{\chi}^2$ as the $1 - \sigma$ uncertainty on our best fit values of thermal inertia and volume
 440 equivalent diameter. As a result we find $\Gamma = 48 \pm 5 J m^{-2} s^{-0.5} K^{-1}$ and $D_V =$
 441 $209 \pm 1 \text{ km}$ as the best fit solution for a model using the convex shape without
 442 roughness; and $\Gamma = 8 \pm 8 J m^{-2} s^{-0.5} K^{-1}$ and $D_V = 194 \pm 2 \text{ km}$ as the best fit
 443 solution for a model using the convex shape with a low roughness.

444 5.2. Non-convex shape model

445 Figure 7 shows our best-fit estimator $\bar{\chi}^2$ of the TPM, calculated in the case
 446 of the non-convex shape.

447

448 **[Fig. 7 here]**

449

450 In this case, a model with a low or medium roughness and a thermal inertia
 451 $< 100 J m^{-2} s^{-0.5} K^{-1}$ gives the best fit to the observations. In particular, the
 452 minima of the ‘low roughness’ and ‘medium roughness’ models are at $\Gamma=9$ and 0
 453 $J m^{-2} s^{-0.5} K^{-1}$, respectively. The corresponding value of D_V are 189 km and
 454 182 km, respectively, with $p_V = 0.07$. The solution with $\Gamma=0 J m^{-2} s^{-0.5} K^{-1}$ is

455 non physical and thus we reject it. Although 100 km-sized Main Belt aster-
 456 oids are known to have low thermal inertia, their values are in general larger
 457 than $10 \text{ J m}^{-2} \text{ s}^{-0.5} \text{ K}^{-1}$ (see e.g., Mueller and Lagerros, 1998, and refer-
 458 ences therein). We also used the Monte-Carlo procedure described above to
 459 estimate the uncertainties on the fit parameters. These uncertainties result to
 460 be of $1 \text{ J m}^{-2} \text{ s}^{-0.5} \text{ K}^{-1}$ for the thermal inertia and 1 km for the volume
 461 equivalent diameter. We show in Fig. 4 the measured fluxes and visibilities of
 462 (41) Daphne along with the best fit of the non-convex case ('low roughness',
 463 $\Gamma = 9 \text{ J m}^{-2} \text{ s}^{-0.5} \text{ K}^{-1}$, $D_V = 189 \text{ km}$, $p_V = 0.070$). Our model, when used
 464 with the non-convex shape, also provides a good match to the observed flux.
 465 We note that the flux prediction at the third epoch is as well higher than the
 466 measured one. This effect may also be due to an underestimation of the source
 467 flux by MIDI, as described above. Moreover, the non-convex model seems to
 468 better fit the measured visibilities than the convex one. This result is consistent
 469 with the fact that the non-convex shape model corresponds to a more realis-
 470 tic and detailed representation of (41) Daphne, as previously indicated by B.
 471 Carry (private communication)³ who better reproduced an occultation profile
 472 of (41) Daphne with this shape model. We can note however a slight mismatch
 473 between the model predictions and the measurements at the fourth epoch. The
 474 mismatch is located around $\frac{B}{\lambda} \approx 6 \text{ as}^{-1}$ (or $\lambda \approx 9.6 \mu\text{m}$) i.e. close to the atmo-
 475 spheric ozone absorption feature. This time-dependent absorption feature can
 476 cause fluctuations and lower the signal to noise ratio on both the coherent flux
 477 and the photometry. Due to its relative variability, this feature is frequently im-
 478 perfectly removed during the reduction process of interferometric observations
 479 (see e.g., Tubbs et al., 2004). All the results are summarized in Table 3.

480

481 [Table 3 here]

482

483 6. Discussion

484 6.1. Size and geometric visible albedo

485 The best-fit value of D_V obtained from our TPM analysis of MIDI data us-
486 ing the non-convex shape model, namely 189 ± 1 km, presents a discrepancy
487 with the nominal value (185 ± 5 km) of about 4 km. This is about 4 times
488 greater than the statistical uncertainties implied by the photometric and vis-
489 ibilities measurements and estimated via our Monte Carlo method. However,
490 this discrepancy represents a relative accuracy of 2% on the diameter that ap-
491 pears remarkably good for a typical size determination of asteroids. If the two
492 equally plausible solutions in terms of our best-fit indicator, i.e. low roughness
493 - $\Gamma=9 J m^{-2} s^{-0.5} K^{-1}$ and medium roughness - $\Gamma=0 J m^{-2} s^{-0.5} K^{-1}$, are
494 considered in order to estimate the model error on the value of D_V , we found
495 that the latter is 7 km i.e. 4% in relative accuracy.

496 When the convex model is used as an *a priori* shape for the TPM, the value
497 of D_V resulting from the analysis of MIDI data is between 194 and 209 km (with
498 a mean value of about 200 km), depending on whether a low-roughness or a no-
499 roughness model, respectively, is assumed for the surface of Daphne. Because
500 both solutions are equally good in terms of our best-fit estimator, it is clear that
501 the systematic model uncertainty dominates the final size determination. This
502 systematic relative uncertainty is of the order of 7% on the diameter.

503 It is also evident that the best fit values of the equivalent volume diameter
504 obtained when using the convex shape are larger than the nominal value of
505 D_V of the non convex shape. This is because the latter has a smaller volume
506 (due to the presence of topographic concavities) for a similar projected size on
507 the plane of the sky. This volume overestimation when the convex shape is
508 used, clearly indicates that the imposed condition of convexity, imposed by the
509 lightcurve inversion technique (see Kaasalainen and Torppa, 2001), introduces
510 a significant systematic bias on the size when large concavities are present on
511 the asteroid surface.

512 The geometric visible albedo values derived from the TPM with the convex

513 and non-convex shapes are in the range between 0.05 and 0.07. This is in
514 agreement with the C-type taxonomic classification of (41) Daphne.

515 6.2. Thermal properties

516 We obtained for the first time good constraints on the determination of
517 macroscopic roughness for both shape models, although the results slightly dif-
518 fer. While a very low roughness is preferred in the convex shape case, a low
519 or moderate roughness gives the best-fit in the case of the non-convex one. We
520 estimate that the corresponding mean surface slope values should lie between
521 10 and 29° for (41) Daphne. A high macroscopic roughness is discarded, which
522 is quite surprising given the important surface roughness expected for large as-
523 teroids. Large main-belt asteroids such as (1) Ceres and (2) Pallas are expected
524 to have rough surfaces as found by Spencer et al. (1989) from the analysis of the
525 thermal infrared emission of these bodies. It is also known that the observed
526 zero-phase thermal emission of the Moon is well reproduced by a rough-surface
527 model, i.e. $\rho_c = 0.64$ and $\gamma_c = 90^\circ$ (Spencer, 1990). The possibility to constrain
528 the macroscopic roughness in the thermal infrared is very interesting because
529 it allows, in principle, a more accurate determination of the asteroids thermal
530 inertia from TPM modeling.

531 Our TPM analysis indicates that (41) Daphne has a thermal inertia value
532 certainly smaller than $50 J m^{-2} s^{-0.5} K^{-1}$, and likely in the range between
533 10 and $\sim 30 J m^{-2} s^{-0.5} K^{-1}$, indicating that a layer of very fine regolith
534 covers its surface. This is in agreement with the thermal inertia values already
535 measured on main-belt asteroids larger than 100 km in diameter. Indeed, from
536 mid- and far-infrared observations, Mueller and Lagerros (1998) derived very
537 low thermal inertia values, between 5 and $25 J m^{-2} s^{-0.5} K^{-1}$, for some large
538 Main Belt asteroids including (1) Ceres, (2) Pallas, (3) Juno, (4) Vesta, and
539 (532) Herculina. Moreover, Müller and Blommaert (2004) derived a thermal
540 inertia of about $15 J m^{-2} s^{-0.5} K^{-1}$ for (65) Cybele. More recently, from the
541 direct measurement of the cooling during shadowing events in a binary system,
542 Mueller et al. (2010) measured a thermal inertia of $20 \pm 15 J m^{-2} s^{-0.5} K^{-1}$ for

543 the large binary Trojan ($D \approx 100$ km), (617) Patroclus.

544

545 Several works were recently devoted to the determination of the thermal
546 inertia value of the asteroids surface from TPM analysis of disk integrated ther-
547 mal infrared data (see e.g., Delbo et al., 2007; Delbo and Tanga, 2009; Mueller,
548 2007, and references therein). In general, these works clearly showed that a
549 good fit of the model to the observations can be obtained by using any rough-
550 ness model. Because the determination of the value of the thermal inertia is a
551 function of the roughness model adopted, any constraint on the latter parameter
552 will allow improving the determination of thermal inertia. In order to show the
553 effect of the visibility on the determination of a simultaneous solution for both
554 thermal inertia and surface roughness, we also performed a TPM analysis of
555 the disk integrated thermal infrared data of (41) Daphne, using the non-convex
556 shape and neglecting the visibility measurements.

557

558 **[Fig. 8 here]**

559

560 As it can be seen from Fig. 8, any roughness model and any value of the
561 thermal inertia give a value of $\bar{\chi}^2$ smaller than 1, which implies that any value
562 of these parameters allows the TPM to fit equally well the infrared flux. In
563 order to reduce this degeneracy, it is known that thermal infrared photometric
564 observations are needed at different illuminations and viewing geometries in
565 order to constrain the asteroids thermal properties from a TPM modeling of
566 photometric observations only.

567 **7. Conclusion**

568 We have obtained the first successful interferometric observations of asteroids
569 in the thermal infrared using the ATs of the ESO VLTI. We observed the asteroid
570 (41) Daphne using the MIDI instrument and the 16m-long baseline E0-G0.

571 We developed a thermophysical model (TPM) for the analysis of interfero-

572 metric observations of asteroids in the thermal infrared, with the aim of deriving
573 information about size and thermal properties.

574 We applied our TPM to the MIDI observations of (41) Daphne: our results
575 indicate that Daphne has a volume equivalent diameter between 194 and 209
576 km, depending on the surface roughness, if a convex shape model derived from
577 lightcurve inversion is used as an *a priori* constraint on the shape of the asteroid.
578 Since the nominal size, attached to the non-convex KOALA model, is 185 ± 5 km
579 (B. Carry, private communication)³, our results confirm that the assumption of
580 convexity introduces a systematic bias on the size determination when important
581 concavities are present on the asteroid’s surface. In contrast, if the non-convex
582 shape model is used, the volume equivalent diameter obtained from the TPM is
583 189 ± 1 km, i.e. very close to the nominal value of 185 ± 5 km. We estimated our
584 model systematic uncertainty to be of 4% and of 7% on the determination of
585 the asteroid volume equivalent diameter depending on whether the non-convex
586 or the convex shape is used, respectively.

587 Our TPM analysis also showed that the macroscopic surface roughness can
588 be constrained by interferometry, thanks to the angular resolving power offered
589 by the VLTI and which allows to resolve the temperature distribution on the
590 asteroid surface. In particular, using both shape models of (41) Daphne, we
591 found a moderate to low roughness (see Table 1); ‘high roughness’ models are
592 discarded by our analysis. With such a constraint on the macroscopic roughness,
593 the TPM results indicate a very low thermal inertia for (41) Daphne, certainly
594 smaller than $50 \text{ J m}^{-2} \text{ s}^{-0.5} \text{ K}^{-1}$. This confirmed previous results indicating
595 that the surface of asteroids with sizes larger than 100 km has a low thermal
596 inertia. As shown by this work, the possibility of constraining the macroscopic
597 roughness is important in the prospect of an accurate modelling of the thermal
598 infrared emission of asteroids, and especially thermal inertia determination (see
599 also Mueller, 2007; Delbo and Tanga, 2009).

Acknowledgments

We would like to thank the staff and the Science Archive Operation of the European Southern Observatory (ESO) for their support in the acquisition of the data. The comments from the referee Benoit Carry and an anonymous referee were extremely helpful in revising this work and allowed us to improve significantly the manuscript.

References

- Bottke, W.F., Durda, D.D., Nesvorný, D., Jedicke, R., Morbidelli, A., Vokrouhlický, D., Levison, H.F., 2005. Linking the collisional history of the main asteroid belt to its dynamical excitation and depletion. *Icarus* 179, 63–94.
- Bottke, Jr., W.F., Vokrouhlický, D., Rubincam, D.P., Nesvorný, D., 2006. The Yarkovsky and Yorp Effects: Implications for Asteroid Dynamics. *Annu. Rev. Earth Planet.* 34, 157–191.
- Bowell, E., Hapke, B., Domingue, D., Lumme, K., Peltoniemi, J., Harris, A.W., 1989. Application of photometric models to asteroids, in: R. P. Binzel, T. Gehrels, & M. S. Matthews (Ed.), *Asteroids II*, pp. 524–556.
- Carry, B., Dumas, C., Kaasalainen, M., Berthier, J., Merline, W.J., Erard, S., Conrad, A., Drummond, J.D., Hestroffer, D., Fulchignoni, M., Fusco, T., 2010. Physical properties of (2) Pallas. *Icarus* 205, 460–472.
- Chesneau, O., 2007. MIDI: Obtaining and analysing interferometric data in the mid-infrared. *New Astron. Rev.* 51, 666–681.
- Christensen, P.R., Bandfield, J.L., Bell, J.F., Gorelick, N., Hamilton, V.E., Ivanov, A., Jakosky, B.M., Kieffer, H.H., Lane, M.D., Malin, M.C., McConnochie, T., McEwen, A.S., McSween, H.Y., Mehall, G.L., Moersch, J.E., Nealon, K.H., Rice, J.W., Richardson, M.I., Ruff, S.W., Smith, M.D., Titus, T.N., Wyatt, M.B., 2003. Morphology and Composition of the Surface of Mars: Mars Odyssey THEMIS Results. *Science* 300, 2056–2061.
- Cohen, J.G., 1999. The Spectra of Main-Sequence Stars in Galactic Globular Clusters. II. CH and CN Bands in M71. *Astron. J.* 117, 2434–2439.
- Daban, J.B., Gouvret, C., Guillot, T., Agabi, A., Crouzet, N., Rivet, J.P., Mekarnia, D., Abe, L., Bondoux, E., Fantei-Caujolle, Y., Fressin, F., Schmider, F.X., Valbousquet, F., Blanc, P.E., Le van Suu, A., Rauer, H., Erikson, A., Pont, F., Aigrain, S., 2010. ASTEP 400: a telescope designed

- for exoplanet transit detection from Dome C, Antarctica, in: Society of Photo-Optical Instrumentation Engineers (SPIE) Conference Series, volume 7733. p. 77334T.
- Delbo, M., Dell’Oro, A., Harris, A.W., Mottola, S., Mueller, M., 2007. Thermal inertia of near-Earth asteroids and implications for the magnitude of the Yarkovsky effect. *Icarus* 190, 236–249.
- Delbo, M., Harris, A.W., 2002. Physical properties of near-Earth asteroids from thermal infrared observations and thermal modeling. *Meteor. and Plan. Sci.* 37, 1929–1936.
- Delbo, M., Ligorì, S., Matter, A., Cellino, A., Berthier, J., 2009. First VLTI-MIDI Direct Determinations of Asteroid Sizes. *Astrophys. J.* 694, 1228–1236.
- Delbo, M., Tanga, P., 2009. Thermal inertia of main belt asteroids smaller than 100 km from IRAS data. *Plan. and Space Sci.* 57, 259–265.
- Descamps, P., Marchis, F., Pollock, J., Berthier, J., Vachier, F., Birlan, M., Kaasalainen, M., Harris, A.W., Wong, M.H., Romanishin, W.J., Cooper, E.M., Kettner, K.A., Wiggins, P., Kryszczyńska, A., Polinska, M., Coliac, J., Devyatkin, A., Verestchagina, I., Gorshanov, D., 2008. New determination of the size and bulk density of the binary Asteroid 22 Kalliope from observations of mutual eclipses. *ICARUS* 196, 578–600.
- Durech, J., Sidorin, V., Kaasalainen, M., 2010. DAMIT: a database of asteroid models. *Astron. and Astrophys.* 513, A46.
- Emery, J.P., Sprague, A.L., Witteborn, F.C., Colwell, J.E., Kozłowski, R.W.H., Wooden, D.H., 1998. Mercury: Thermal Modeling and Mid-infrared (5-12 μm) Observations. *Icarus* 136, 104–123.
- Giorgini, J.D., Ostro, S.J., Benner, L.A.M., Chodas, P.W., Chesley, S.R., Hudson, R.S., Nolan, M.C., Klemola, A.R., Standish, E.M., Jurgens, R.F., Rose, R., Chamberlin, A.B., Yeomans, D.K., Margot, J.L., 2002. Asteroid 1950

- DA's Encounter with Earth in 2880: Physical Limits of Collision Probability Prediction. *Science* 296, 132–136.
- Hapke, B., 1984. Bidirectional reflectance spectroscopy. III - Correction for macroscopic roughness. *Icarus* 59, 41–59.
- Harris, A.W., Lagerros, J.S.V., 2002. Asteroids in the Thermal Infrared. *Asteroids III* , 205–218.
- Hestroffer, D., Tanga, P., Cellino, A., Guglielmetti, F., Lattanzi, M., Di Martino, M., Zappalà, V., Berthier, J., 2002. Asteroids observations with the Hubble Space Telescope. I. Observing strategy, and data analysis and modeling process. *Astron. and Astrophys.* 391, 1123–1132.
- Jakosky, B.M., 1986. On the thermal properties of Martian fines. *Icarus* 66, 117–124.
- Kaasalainen, M., 2011. Maximum compatibility estimates and shape reconstruction with boundary curves and volumes of generalized projections. *Inv. Prob. and Imag.*, submitted .
- Kaasalainen, M., Mottola, S., Fulchignoni, M., 2002. Asteroid Models from Disk-integrated Data. *Asteroids III* , 139–150.
- Kaasalainen, M., Torppa, J., 2001. Optimization Methods for Asteroid Lightcurve Inversion. I. Shape Determination. *Icarus* 153, 24–36.
- Lagerros, J.S.V., 1998. Thermal physics of asteroids. IV. Thermal infrared beaming. *Astron. and Astrophys.* 332, 1123–1132.
- Leinert, C., Graser, U., Przygodda, F., Waters, L.B.F.M., Perrin, G., Jaffe, W., Lopez, B., Bakker, E.J., Böhm, A., Chesneau, O., Cotton, W.D., Damstra, S., de Jong, J., Glazenberg-Kluttig, A.W., Grimm, B., Hanenburg, H., Laun, W., Lenzen, R., Ligorì, S., Mathar, R.J., Meisner, J., Morel, S., Morr, W., Neumann, U., Pel, J.W., Schuller, P., Rohloff, R.R., Stecklum, B., Storz, C.,

- von der Lühe, O., Wagner, K., 2003. MIDI - the 10 μm instrument on the VLTI. *Astrophys. and Space Sci.* 286, 73–83.
- Milani, A., Chesley, S.R., Sansaturio, M.E., Bernardi, F., Valsecchi, G.B., Arratia, O., 2009. Long term impact risk for (101955) 1999 RQ₃₆. *Icarus* 203, 460–471.
- Morbidelli, A., Vokrouhlický, D., 2003. The Yarkovsky-driven origin of near-Earth asteroids. *ICARUS* 163, 120–134.
- Mouret, S., Hestroffer, D., Mignard, F., 2007. Asteroid masses and improvement with Gaia. *Astron. and Astrophys.* 472, 1017–1027.
- Mueller, M., 2007. Surface properties of asteroids from mid-infrared observations and thermophysical modeling. Ph.D. thesis. Freie Universitaet Berlin.
- Mueller, M., Marchis, F., Emery, J.P., Harris, A.W., Mottola, S., Hestroffer, D., Berthier, J., di Martino, M., 2010. Eclipsing binary Trojan asteroid Patroclus: Thermal inertia from Spitzer observations. *Icarus* 205, 505–515. 0908.4198.
- Mueller, T.G., Lagerros, J.S.V., 1998. Asteroids as far-infrared photometric standards for ISOPHOT. *Astron. and Astrophys.* 338, 340–352.
- Müller, T.G., Barnes, P.J., 2007. 3.2 mm lightcurve observations of (4) Vesta and (9) Metis with the Australia Telescope Compact Array. *Astron. and Astrophys.* 467, 737–747.
- Müller, T.G., Blommaert, J.A.D.L., 2004. λ ASTROBJ λ 65 Cybele λ /ASTROBJ λ in the thermal infrared: Multiple observations and thermophysical analysis. *Astron. and Astrophys.* 418, 347–356. [arXiv:astro-ph/0401458](https://arxiv.org/abs/astro-ph/0401458).
- Nesvorný, D., Bottke, W.F., 2004. Detection of the Yarkovsky effect for main-belt asteroids. *Icarus* 170, 324–342.
- Ostro, S.J., Hudson, R.S., Nolan, M.C., Margot, J., Scheeres, D.J., Campbell, D.B., Magri, C., Giorgini, J.D., Yeomans, D.K., 2000. Radar Observations of Asteroid 216 Kleopatra. *Science* 288, 836–839.

- Perrin, G., Leinert, C., Graser, U., Waters, L.B.F.M., Lopez, B., 2003. MIDI, the 10 μm interferometer of the VLT, in: G. Perrin & F. Malbet (Ed.), EAS Publications Series, volume 6. p. 127.
- Przygodda, F., Chesneau, O., Graser, U., Leinert, C., Morel, S., 2003. Interferometric Observation at Mid-Infrared Wave-lengths with MIDI. *Astrophys. and Space Sci.* 286, 85–91.
- Spencer, J.R., 1990. A rough-surface thermophysical model for airless planets. *ICARUS* 83, 27–38.
- Spencer, J.R., Lebofsky, L.A., Sykes, M.V., 1989. Systematic biases in radiometric diameter determinations. *ICARUS* 78, 337–354.
- Stuart, J.S., Binzel, R.P., 2004. Bias-corrected population, size distribution, and impact hazard for the near-Earth objects. *ICARUS* 170, 295–311.
- Tanga, P., Comito, C., Paolicchi, P., Hestroffer, D., Cellino, A., Dell’Oro, A., Richardson, D.C., Walsh, K.J., Delbo, M., 2009. Rubble-Pile Reshaping Reproduces Overall Asteroid Shapes. *Astrophys. J.* 706, L197–L202.
- Tanga, P., Hestroffer, D., Berthier, J., Cellino, A., Lattanzi, M.G., di Martino, M., Zappalà, V., 2001. HST/FGS Observations of the Asteroid (216) Kleopatra. *Icarus* 153, 451–454.
- Tanga, P., Hestroffer, D., Cellino, A., Lattanzi, M., Di Martino, M., Zappalà, V., 2003. Asteroid observations with the Hubble Space Telescope. II. Duplicity search and size measurements for 6 asteroids. *Astron. and Astrophys.* 401, 733–741.
- Tedesco, E.F., Williams, J.G., Matson, D.L., Weeder, G.J., Gradie, J.C., Lebofsky, L.A., 1989. A three-parameter asteroid taxonomy. *Astron. J.* 97, 580–606.
- Thomas, P.C., Joseph, J., Carcich, B., Veverka, J., Clark, B.E., Bell, J.F., Byrd, A.W., Chomko, R., Robinson, M., Murchie, S., Prockter, L., Cheng, A., Izenberg, N., Malin, M., Chapman, C., McFadden, L.A., Kirk, R., Gaffey,

- M., Lucey, P.G., 2002. Eros: Shape, Topography, and Slope Processes. *Icarus* 155, 18–37.
- Thomas, P.C., Veverka, J., Bell, J.F., Clark, B.E., Carcich, B., Joseph, J., Robinson, M., McFadden, L.A., Malin, M.C., Chapman, C.R., Merline, W., Murchie, S., 1999. Mathilde: Size, Shape, and Geology. *Icarus* 140, 17–27.
- Tubbs, R.N., Meisner, J.A., Bakker, E.J., Albrecht, S., 2004. Differential phase delay observations with VLTI-MIDI at N-band, in: W. A. Traub (Ed.), *Society of Photo-Optical Instrumentation Engineers (SPIE) Conference Series*, volume 5491. p. 588.
- Veverka, J., Farquhar, B., Robinson, M., Thomas, P., Murchie, S., Harch, A., Antreasian, P.G., Chesley, S.R., Miller, J.K., Owen, W.M., Williams, B.G., Yeomans, D., Dunham, D., Heyler, G., Holdridge, M., Nelson, R.L., Whittenburg, K.E., Ray, J.C., Carcich, B., Cheng, A., Chapman, C., Bell, J.F., Bell, M., Bussey, B., Clark, B., Domingue, D., Gaffey, M.J., Hawkins, E., Izenberg, N., Joseph, J., Kirk, R., Lucey, P., Malin, M., McFadden, L., Merline, W.J., Peterson, C., Prockter, L., Warren, J., Wellnitz, D., 2001a. The landing of the NEAR-Shoemaker spacecraft on asteroid 433 Eros. *Nature* 413, 390–393.
- Veverka, J., Thomas, P.C., Robinson, M., Murchie, S., Chapman, C., Bell, M., Harch, A., Merline, W.J., Bell, J.F., Bussey, B., Carcich, B., Cheng, A., Clark, B., Domingue, D., Dunham, D., Farquhar, R., Gaffey, M.J., Hawkins, E., Izenberg, N., Joseph, J., Kirk, R., Li, H., Lucey, P., Malin, M., McFadden, L., Miller, J.K., Owen, W.M., Peterson, C., Prockter, L., Warren, J., Wellnitz, D., Williams, B.G., Yeomans, D.K., 2001b. Imaging of Small-Scale Features on 433 Eros from NEAR: Evidence for a Complex Regolith. *Science* 292, 484–488.
- Yano, H., Kubota, T., Miyamoto, H., Okada, T., Scheeres, D., Takagi, Y., Yoshida, K., Abe, M., Abe, S., Barnouin-Jha, O., Fujiwara, A., Hasegawa, S., Hashimoto, T., Ishiguro, M., Kato, M., Kawaguchi, J., Mukai, T., Saito,

J., Sasaki, S., Yoshikawa, M., 2006. Touchdown of the Hayabusa Spacecraft at the Muses Sea on Itokawa. *Science* 312, 1350–1353.

Tables and Table Captions

Roughness model	γ_c	ρ_c	$\bar{\theta}$
no roughness	0°	0.0	0°
low roughness	45°	0.5	10°
medium roughness	68°	0.8	29°
high roughness	90°	1.0	58°

Table 1: The four roughness models used in the application of the TPM to the MIDI data; γ_c and ρ_c respectively correspond to the crater opening angle and the crater density, while $\bar{\theta}$ is the corresponding mean surface slope according to the parameterization introduced by Hapke (1984) (see text and also Delbo et al., 2007, for further details).

Date	UT	r (AU)	Δ (AU)	α (deg)	B (m)	PA (deg)	Tag
2008-03-12	05:19:14	2.0866	1.1920	15.8	13.6	66.6	D ₁
2008-03-12	06:24:35	2.0864	1.1917	15.8	15.4	70.6	D ₂
2008-03-14	04:19:27	2.0834	1.1769	15.0	11.6	61.6	D ₃
2008-03-14	04:32:48	2.0834	1.1769	15.0	12.2	63.4	D ₄

Table 2: Observational circumstances and interferometric parameters of the (41) Daphne observations. r and Δ are the heliocentric and geocentric distances, respectively, while α is the solar phase angle. B and PA are respectively the length and the position angle of the baseline projected on sky. The last column contains a tag associated with each observation.

Shape	Roughness model	$\bar{\chi}^2$	Γ ($J m^{-2} s^{-0.5} K^{-1}$)	D_V (km)	p_V
Convex	No roughness	3.5 ± 0.3	48 ± 6	209 ± 1	0.057 ± 0.009
	Low roughness	3.7 ± 0.3	8_{-8}^{+10}	194 ± 2	0.067 ± 0.011
Non-convex	Low roughness	3.4 ± 0.3	9 ± 1	189 ± 1	0.070 ± 0.011

Table 3: Results of the determination of physical properties of the asteroid (41) Daphne, using the TPM. The $\bar{\chi}^2$ is our best-fit estimator as described by Eq 2; Γ is the thermal inertia, D_V is the spherical volume equivalent diameter, and p_V is the geometric visible albedo. The errors are within 1- σ .

Figure captions and figures

Fig 1 caption :

Image of the asteroid (41) Daphne created from the TPM, using the convex shape model (left image) and the non-convex one (right image). The gray level is proportional to the emitted thermal infrared flux.

Fig 2 caption :

Illustration of the geometric parameters involved in the calculation of the synthetic visibility and flux from a TPM image.

Fig 3 caption :

Left panels: measured thermal infrared fluxes (with error bars) between 8 and 13 μm of (41) Daphne, and the corresponding best-fit synthetic infrared fluxes (solid lines) derived from the TPM in the case of the convex shape; right panels: measured interferometric visibilities plotted, in N band, as a function of angular frequency, and the corresponding synthetic visibilities of the TPM (solid lines). The best-fit model represented here is : ‘no roughness’, $\Gamma = 48 \text{ J m}^{-2} \text{ s}^{-0.5} \text{ K}^{-1}$. The tags D_1 , D_2 , D_3 and D_4 indicate the observing epoch in the chronological order (see Table 2).

Fig 4 caption :

As for Fig. 3, but the best-fit model represented here, in the case of the non-convex shape, is : ‘low roughness’, $\Gamma = 9 \text{ J m}^{-2} \text{ s}^{-0.5} \text{ K}^{-1}$. The tags D_1 , D_2 , D_3 and D_4 indicate the observing epoch in the chronological order (see Table 2).

Fig 5 caption :

Diamonds: lightcurve obtained from CCD photometric observations in the visible of (41) Daphne in October 2009 during the tests of the ASTEP 0.4 m telescope at the Observatoire de la Côte d’Azur, Nice, France. These observations spanned a period of about 3 hours. Solid curve: corresponding best-fit lightcurve from the convex model.

Fig 6 caption :

Plot of $\bar{\chi}^2$ (see Eq. 2), calculated from the TPM in the case of the convex shape, as a function of thermal inertia Γ , for the four roughness models (see Table 1).

Fig 7 caption :

Plot of $\bar{\chi}^2$ (see Eq. 2), calculated from the TPM in the case of the non-convex shape, as a function of thermal inertia Γ , for the four roughness models (see Table 1).

Fig 8 caption :

Plot of $\bar{\chi}^2$ (see Eq. 2) calculated from the TPM, using only the flux measurements of (41) Daphne. This is represented in the case of the non-convex shape, as a function of thermal inertia Γ , for the four roughness models (see Table 1).

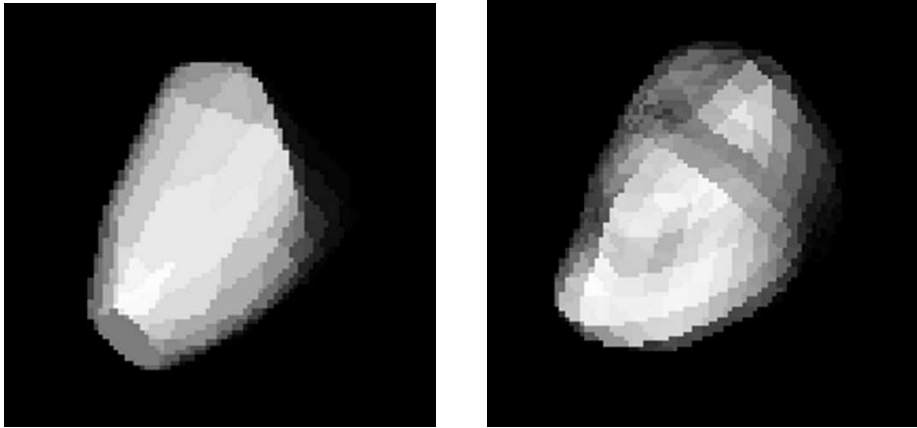


Figure 1:

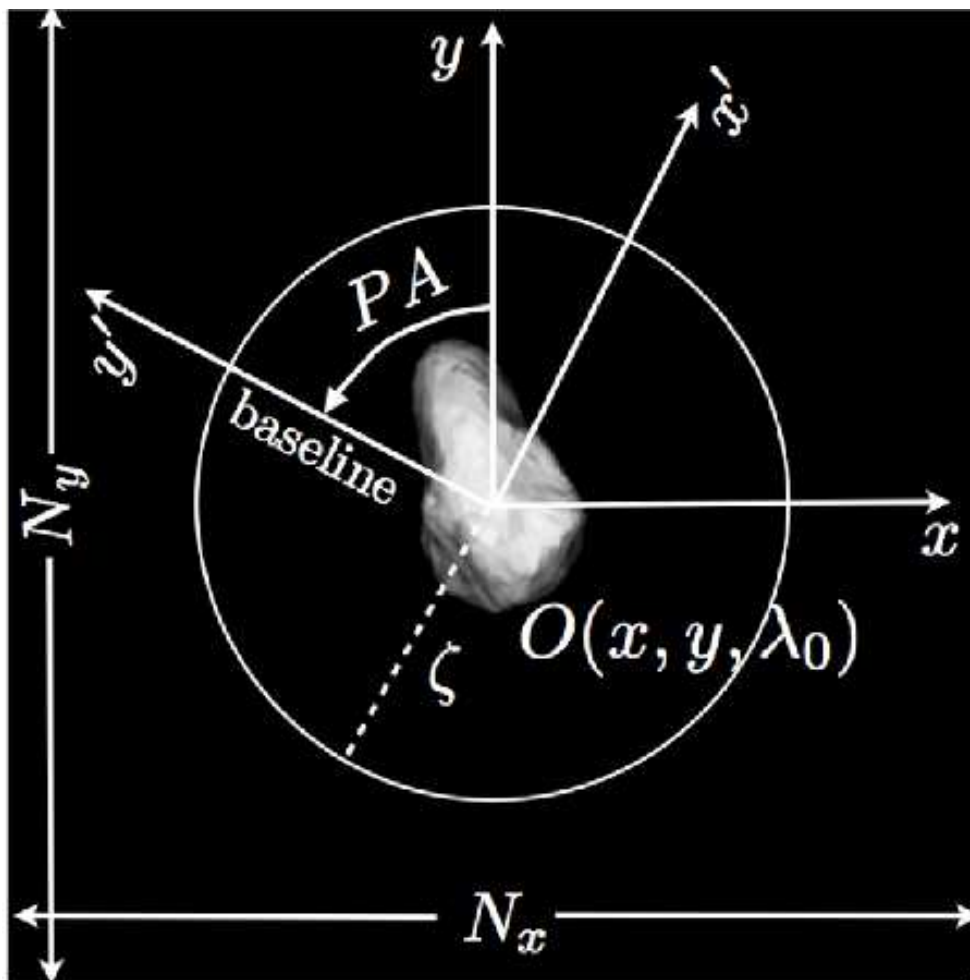


Figure 2:

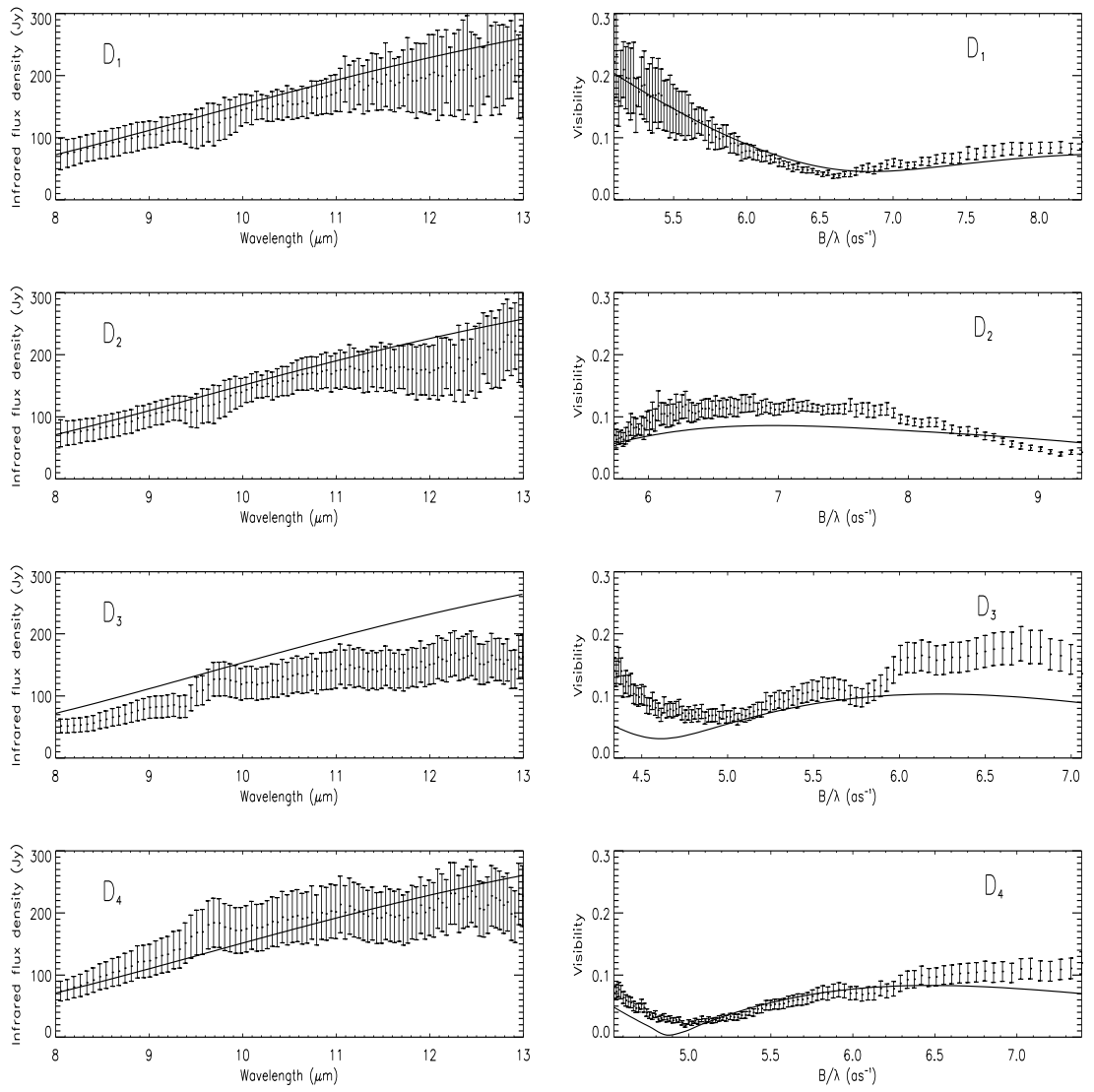


Figure 3:

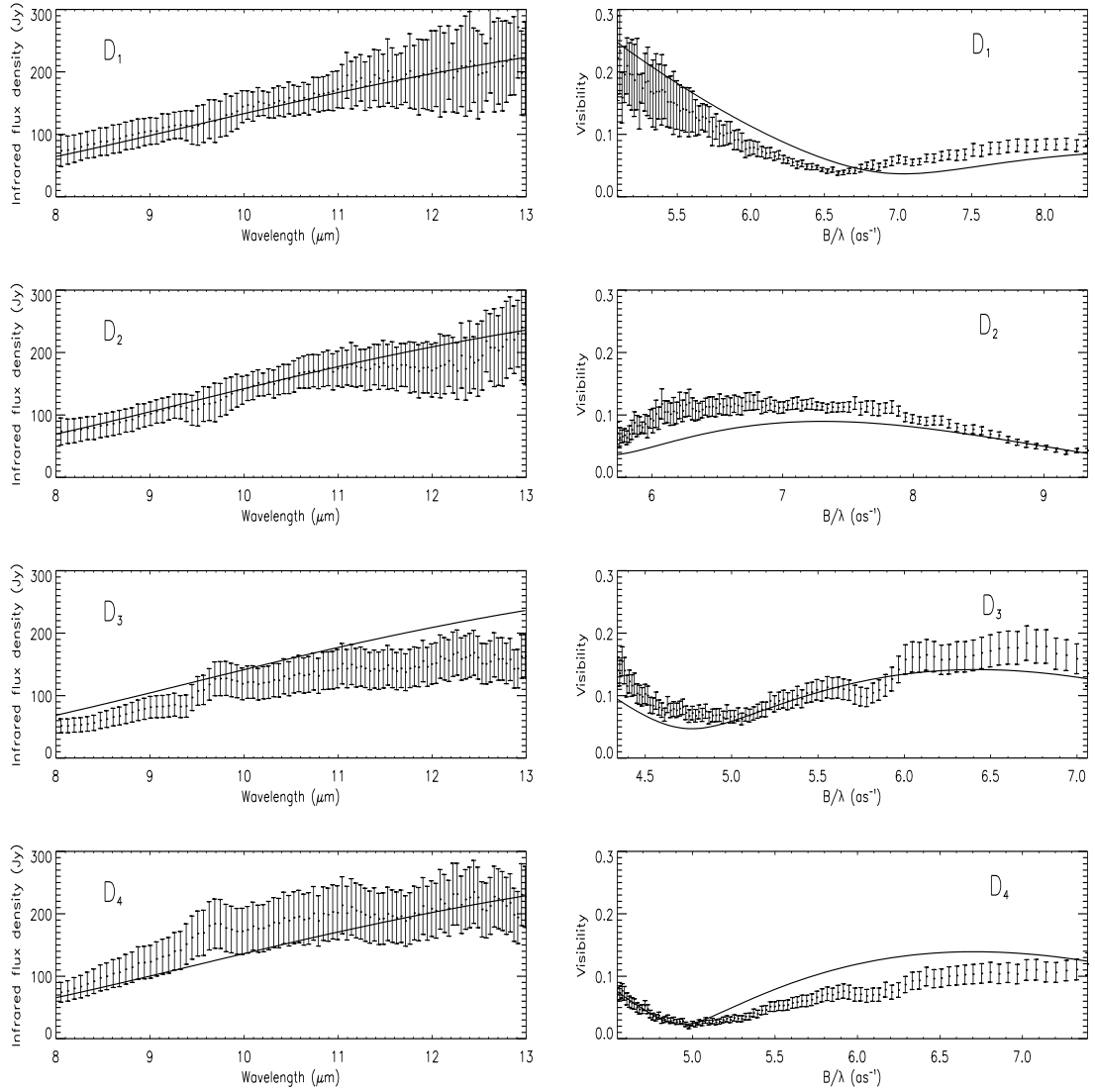


Figure 4:

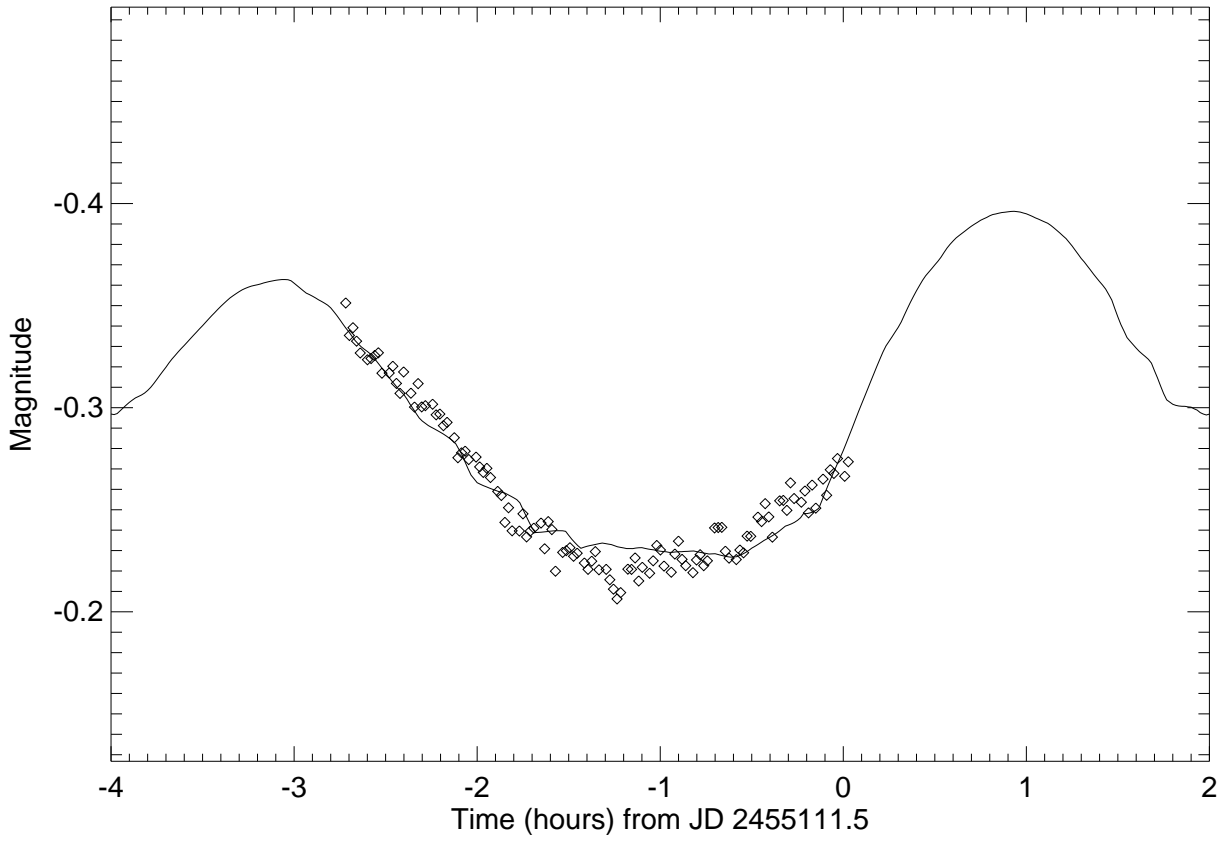


Figure 5:

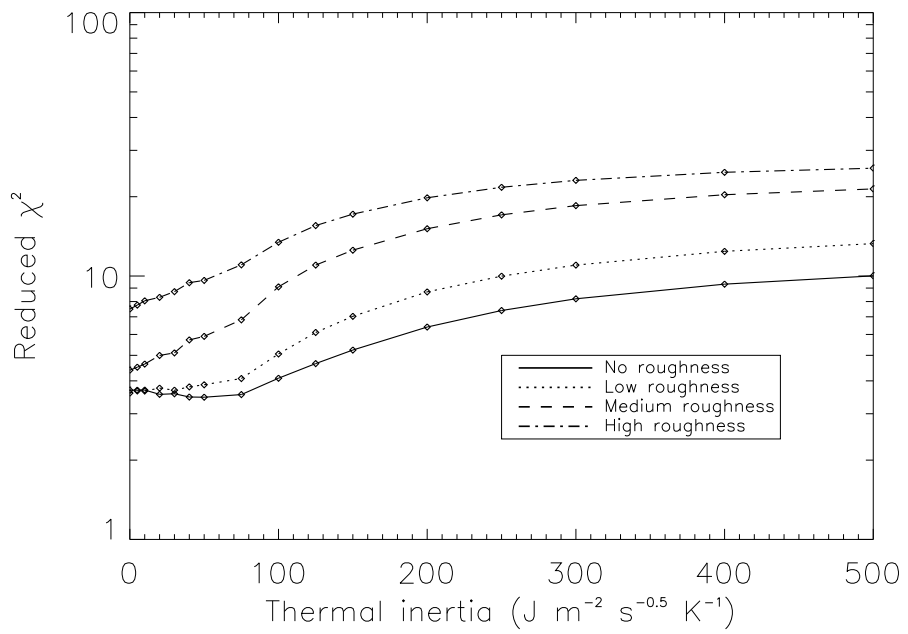


Figure 6:

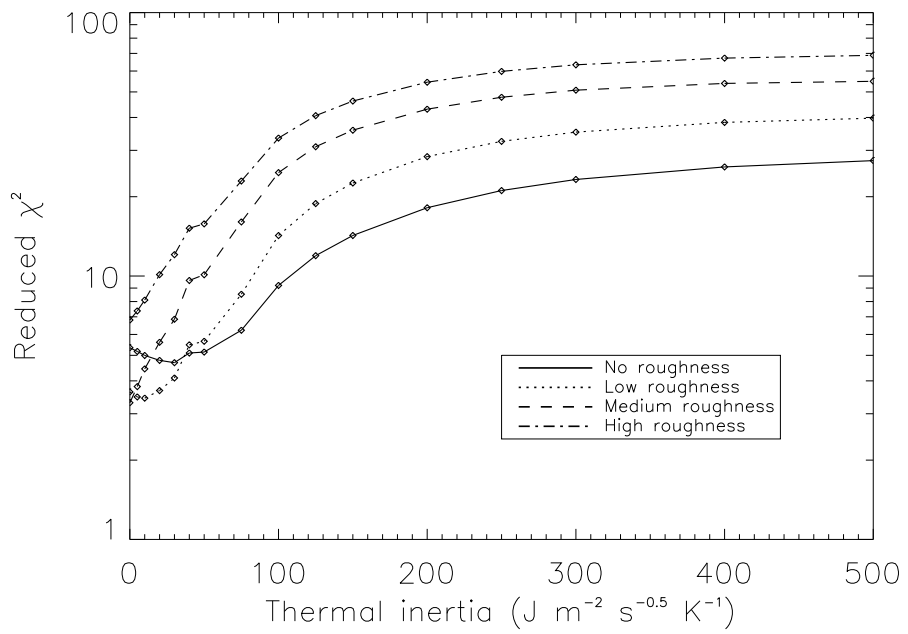


Figure 7:

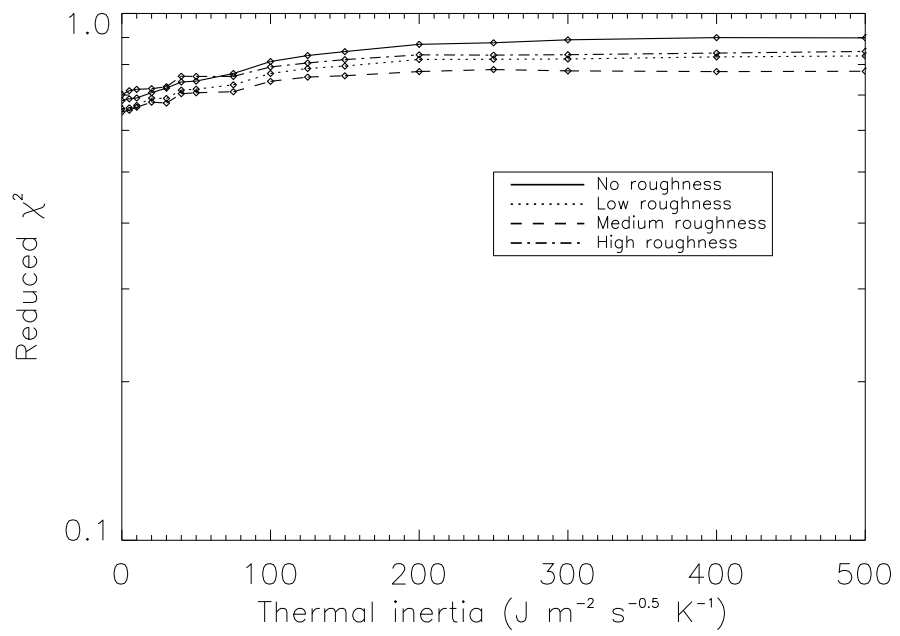


Figure 8: